

Full length article

Multiple mechanisms of lath martensite plasticity

L. Morsdorf^a, O. Jeannin^a, D. Barbier^b, M. Mitsuhashi^c, D. Raabe^a, C.C. Tasan^{d,*}^a Max-Planck-Institut für Eisenforschung, Max-Planck-Straße 1, 40237 Düsseldorf, Germany^b ArcelorMittal Research and Development, Voie Romaine-BP30320, 57283 Maizières-lès-Metz, Cedex, France^c Department of Engineering Sciences for Electronics and Materials, Kyushu University, 6-1 Kasugakoen, Kasuga, Fukuoka, 816-8580, Japan^d Department of Materials Science and Engineering, Massachusetts Institute of Technology, 77 Massachusetts Avenue, Cambridge, MA 02139, USA

ARTICLE INFO

Article history:

Received 4 July 2016

Received in revised form

2 September 2016

Accepted 5 September 2016

Available online 16 September 2016

Keywords:

EBSD

Austenite

Micro-mechanics

Strain mapping

DIC

ABSTRACT

The multi-scale complexity of lath martensitic microstructures requires scale-bridging analyses to better understand the deformation mechanisms activated therein. In this study, plasticity in lath martensite is investigated by multi-field mapping of deformation-induced microstructure, topography, and strain evolution at different spatial resolution vs. field-of-view combinations. These investigations reveal site-specific initiation of dislocation activity within laths, as well as significant plastic accommodation in the vicinity of high angle block and packet boundaries. The observation of interface plasticity raises several questions regarding the role of thin inter-lath austenite films. Thus, accompanying transmission electron microscopy and synchrotron x-ray diffraction experiments are carried out to investigate the stability of these films to mechanical loading, and to discuss alternative boundary sliding mechanisms to explain the observed interface strain localization.

© 2016 Acta Materialia Inc. Published by Elsevier Ltd. All rights reserved.

1. Introduction

Martensite as a phase is known for its strength and hardness, but not for its ductility. Yet, this crucial constituent of high strength steels does exhibit some level of plastic accommodation, depending on composition [1–5] and thermomechanical treatment history [6–9]. This report aims at extending the current understanding on the micro- and nano-scale deformation mechanisms in lath martensite. The long-term goal of the presented work is to lay foundations for the design of tough, as-quenched lath martensitic steels.

We begin with a brief overview of recent developments in the understanding of lath martensitic structures in steels, since deformation mechanisms are strongly connected to these characteristics. The works of Morito et al. [10,11] and Kitahara et al. [12] introduced the crystallographic hierarchy of lath martensite based on the Kurdjumov-Sachs (K-S) orientation relationship [13] between martensite and prior austenite; $\{110\}_{\alpha'} \parallel \{111\}_{\gamma}$, $\langle 111 \rangle_{\alpha'} \parallel \langle 110 \rangle_{\gamma}$. The 24 possible variants are grouped into four packets, including six variants sharing the same $\{110\}$ habit plane, and are further subdivided into blocks separated by high-angle boundaries, sub-

blocks and low-misoriented laths. Accordingly, the austenite transforms into thin lath-shaped crystals in between planar interfaces parallel to the $\{110\}_{\alpha'}$ habit plane resulting in a locally anisotropic microstructure, as summarized in Fig. 1. In contrast to equiaxed grains, the extension of laths is restricted in one dimension resulting in a stack of virtually single crystals with thicknesses limited to ~200 nm [14]. The shear deformation involved in martensitic transformation causes a severely dislocated lath structure, which is initially supersaturated with interstitial carbon. Relaxation processes inevitably occur even upon quenching, leading to some degree of (auto-) tempering effects in the as-quenched microstructure [4,15–17].

As a result of these processes and conditions, lath martensitic microstructures exhibit crystallographic, compositional and morphological heterogeneities induced during the course of martensitic transformation from M_s to M_f [15], which are schematically illustrated in Fig. 1. For example, early transforming coarse laths with relatively low dislocation densities (see insets of dislocation networks) are subjected to more extensive auto-tempering during the quenching process (see insets of carbon distribution maps) in comparison to later transforming thinner laths [15]. From a plasticity viewpoint, these heterogeneities (as well as residual stress distribution heterogeneity [9]) should create a scatter in local yield strength even within the bounds of a single prior austenite grain [15,18,19]. Simultaneous presence of several

* Corresponding author.

E-mail address: tasan@mit.edu (C.C. Tasan).

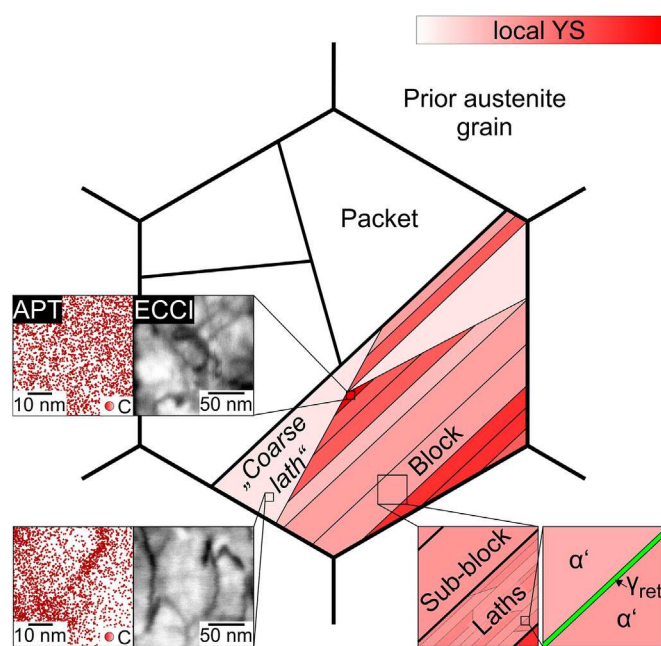


Fig. 1. As-quenched lath martensite microstructure schematically illustrating the crystallographic and topological hierarchy ranging from prior austenite grains to packets, blocks, sub-blocks and laths [10]. Color-code schematically represents possible variations in local yield strength (YS) due to lath size, defect density (see dislocations revealed by electron channeling contrast imaging in the inset) and interstitial carbon content (see atom maps revealed by atom probe tomography analysis in the inset) [15].

further strengthening mechanisms such as solid solution hardening [20] including carbon Cottrell atmosphere effects [21], early stage carbide precipitation [22] and defect interactions [23] explain the martensite's high base strength.

Several studies focused on revealing microstructure-property relationships in lath martensitic steels [24–27]. Since martensite blocks are separated by high angle grain boundaries restricting slip transmission, the effective grain size in martensitic microstructures is usually defined as the block size [24]. This was confirmed by micro-bending tests differentiating low-angle slip transmission and high-angle dislocation pile-up behavior by slip trace analysis [25]. Also, Ghassemi-Armaki et al. found an increase in local strain hardening due to the presence of block boundaries in micro-pillar compression tests [26]. Sub-block boundaries also contribute to boundary strengthening [27].

Considering the bcc slip systems $\{110\}\langle 111 \rangle$ and $\{211\}\langle 111 \rangle$ [28], together with the geometric lath constraints, leads to the classification of in-lath- and out-of-lath-plane slip. In fact, slip on the $\{110\}$ habit plane with two possible $\langle 111 \rangle$ slip directions intrinsically proceeds parallel to the lath interfaces. The preferential activation of in-lath-plane slip was revealed by in-situ electron backscatter diffraction (EBSD) analyses during tensile deformation by Michiuchi et al. [29], who compared the experimentally observed crystal rotations to predictions by the Sachs- and Taylor model. Nambu et al. described a transition in slip behavior during plastic deformation with first the activation of in-lath-plane slip systems followed by transgranular slip after the transition point, which was observed as a slope change in the true stress-strain curve [30]. Mine et al. subscribed lower critical resolved shear stresses to activate the in-lath-plane slip system as analyzed from micro-tensile tests probing specific morphological and crystallographic orientations in lath martensite [31]. In essence, slip plays an important role in the plastic deformation of low-carbon lath martensite while it is being altered by the morphological and crystallographic constraints given by the hierarchical microstructures.

A number of studies recently showed that the presence of a small fraction of austenite, retained in between martensite laths as thin films even in low-carbon low alloyed steels [32–34] (see Fig. 1), may have an influence in the plasticity of martensite [35–37]. Maresca et al. could reproduce the tensile behavior of lath martensite by incorporating the austenitic phase in crystal plasticity simulations. The results were validated with experimental data from Mine et al. and the model also incorporated the constrained slip activity in lath martensite [36]. Owing to the orientation relationship between martensite and retained austenite, one $\{111\}$ slip plane in the austenite thin film is intrinsically parallel to the interfacial habit plane, so that the austenite potentially acts as a 'greasy film' in the deformation process [35].

Experimental evidence for this kind of interface plasticity is presently very rare. A recent micro-tensile study by Du et al. revealed sliding of lath martensite substructure boundaries during deformation, which was suggested to be enabled by the presence of thin film retained austenite [38]. On the other hand, Morito et al. found indications for the transformation of retained austenite at low strain levels to similarly oriented fresh martensite by transmission electron microscopy (TEM) analyses [32,39]. Interestingly, Ohmura et al. observed dislocation absorption at a block boundary by in-situ indentation in TEM and suggested a boundary sliding mechanism owing to the $\{110\}$ nature of martensite interfaces which naturally correspond to the dominant slip plane [40].

The studies suggest that - besides conventional dislocation gliding - interface plasticity requires more attention to completely understand the mechanisms governing lath martensite deformation. The motivation comes not only from the naturally high interface density in martensitic steels, but also from the crystallographically determined character of the different types of interfaces and the presence of a second phase at the interface. With this report we aim at clarifying the occurrence and origin of interface plasticity and its interaction with slip processes in the interface-free martensitic zones and the effect of initial microstructure heterogeneity on these deformation mechanisms.

2. Experimental

Two model low-carbon alloys with compositions Fe-0.13C-5.1Ni and Fe-0.30C-5Ni (wt%) were provided by ArcelorMittal Research in Maizières in form of cold-rolled sheet material. The addition of ~5 wt% Ni promotes enhanced ductility to facilitate the investigation of martensite plasticity. The macroscopic tensile properties in terms of yield strength, tensile strength and elongation to failure are $949 \text{ MPa} \pm 29 \text{ MPa}$, $1239 \text{ MPa} \pm 19 \text{ MPa}$, $13.2\% \pm 0.4\%$ for Fe-0.13C-5.1Ni and $1308 \text{ MPa} \pm 28 \text{ MPa}$, $1886 \text{ MPa} \pm 49 \text{ MPa}$, 7.5% for Fe-0.30C-5Ni. Lath martensitic microstructures were obtained by austenitization treatment for 5 min at 900°C and subsequent water-quenching. Samples for tensile and bending tests were cut and subjected to a metallographic preparation routine including grinding and polishing in order to allow for surface observations. Three sample surface conditions were used for the subsequent characterization tests. One set of tensile samples was etched in 1% Nital; another set was decorated with a single layer of SiO_2 particles [41]; and the bending sample was used in the as-polished condition. These surface conditions enable a multi-scale characterization approach of the bulk martensite deformation response with large field-of-view strain mapping, high resolution strain mapping and trace analysis, respectively. The combination of strain mapping with topographic surface observations allows analyzing both, the in-plane and out-of-plane strain components on the sample surface.

Fig. 2 shows these surface states respectively (see the insets), and the applied stepwise deformation procedure imposed using a

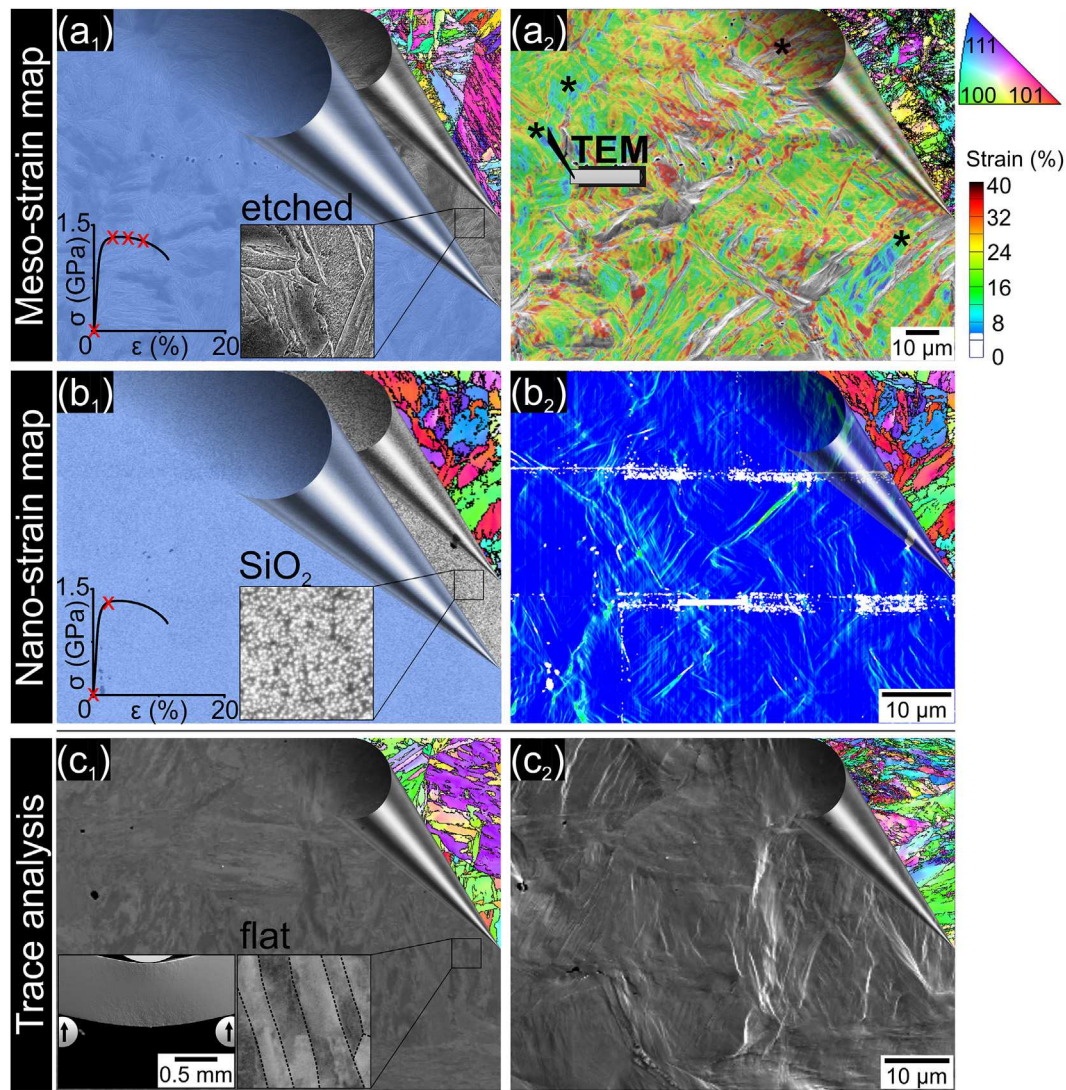


Fig. 2. Methodological overview about the applied multi-scale deformation analysis. Etched (a1), SiO₂ decorated (b1) and flat (c1) surface conditions of tensile/bending samples allow for meso- (a2) and nano-strain (b2) mapping, as well as for surface trace analysis (c2). Red crosses on the continuous tensile curves in the insets of a1 and b1 schematically show the interruption points for image acquisition; bending deformation (inset of c1) is applied stepwise without unloading. Correlative EBSD analysis is carried out prior and after deformation indicated by underlay of inverse pole figure maps (in (c) after slight repolishing). EBSD: electron backscatter diffraction. (For interpretation of the references to colour in this figure legend, the reader is referred to the web version of this article.)

Kammrath & Weiss tensile stage. The ‘field-of-view’ sample was stepwise deformed to 3.7%, 12.2% and 18.9% average local strain levels in the area of interest (Fig. 2a1), the ‘high resolution’ sample was deformed to 2.8% average local strain followed by secondary electron (SE) imaging of the SiO₂ pattern (Fig. 2b1). The as-polished sample was deformed by an in-house made 3-point bending setup.

SE imaging was carried out using a Zeiss 1540XB Crossbeam scanning electron microscope (SEM) operated at 30 kV. SE imaging on the same microstructural position was repeated at every deformation step. The SE images were correlated using digital image correlation (DIC) in the ARAMIS software to obtain the corresponding strain evolution. The strain maps are presented for the last deformation step in Fig. 2a2 and b2. Note that the tensile load was applied in horizontal direction. SE and electron channeling contrast imaging (ECCI) for bending experiments were carried out using a Zeiss ‘Merlin’ SEM at 30 kV.

Before and after complete deformation, EBSD was carried out on the same microstructural positions as observed with SE imaging during deformation, which is also shown in Fig. 2. EBSD with

30–50 nm step size was conducted using a Zeiss 1540XB Crossbeam SEM and a Jeol 6500F SEM operated at 30 kV. Reconstruction of the prior austenite grain structures is achieved by the ARPGE software [42]. For automated analysis of highest Schmid factor slip systems the STABIX matlab toolbox was used [43].

After deformation thin foil specimens are extracted by focused ion beam (FIB) lift-out technique with respect to different local strain levels shown with star marks in Fig. 2a2. A Dual-Beam FEI FIB Helios Nanolab was used for the lift-out and thinning procedure. Transmission Kikuchi diffraction measurements for orientation mapping on the thin foil specimens were carried out using a FEI dual-beam microscope operated at 25 kV with 13 nA current. For subsequent TEM analyses a JEOL JEM-ARM200F microscope was used operated at 200 kV.

Synchrotron x-ray diffraction (s-XRD) measurements were carried out in transmission mode on fractured tensile samples in order to obtain diffraction profiles at different local strain levels. The strain distribution during tensile testing was observed by optical DIC based on spray coating. In the synchrotron measurements, the

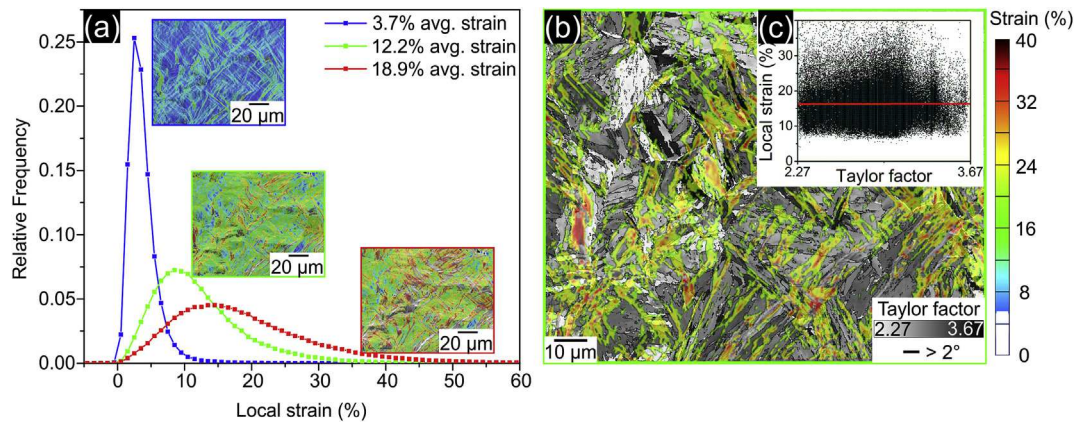


Fig. 3. (a) Strain distribution at three tensile deformation steps; (b) thresholded strain map (>20%) obtained at the second deformation step overlaid to a Taylor factor map from EBSD analysis; (c) correlation of data points plotted as Taylor factor against local strain value with red line showing the linear regression with slope ~ 0 . EBSD: electron backscatter diffraction. (For interpretation of the references to colour in this figure legend, the reader is referred to the web version of this article.)

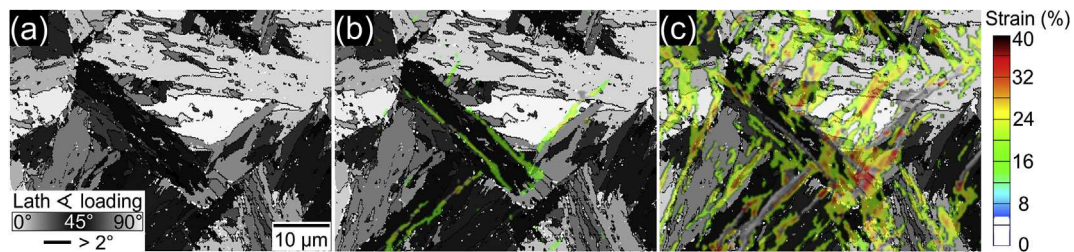


Fig. 4. (a) Geometric orientation of the lath longitudinal direction with respect to horizontal tensile axis in the undeformed microstructure; (b) and (c) show the overlay of the thresholded strain map (>20%) in the initial two deformation steps.

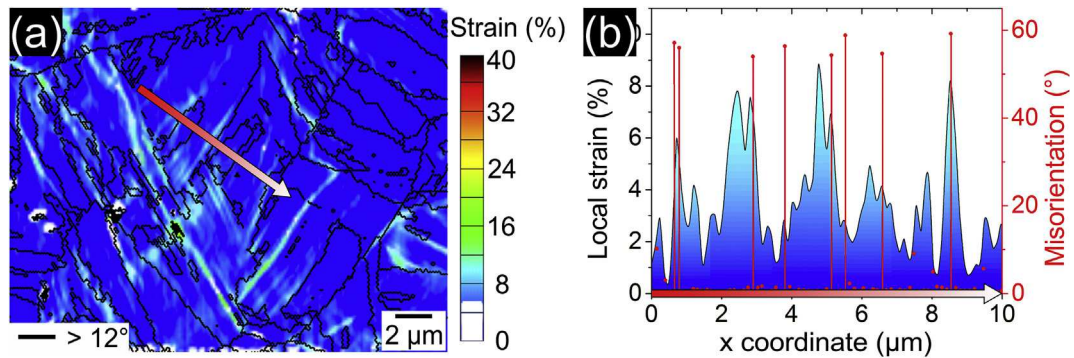


Fig. 5. (a) Overlay of high angle boundaries (>12% misorientation) to high resolution strain map showing the region of \sim one prior austenite grain; (b) correlated strain and misorientation profile along arrow in (a).

beam was aligned with respect to the strain gradient along the sample axis (also schematically shown in Fig. 12b1). The European Synchrotron Radiation Facility (ESRF) in Grenoble was used for experiments with 1 mm beam diameter and 60.025 keV beam energy ($\lambda = 0.0207$ nm).

3. Results

3.1. Strain localization

We first analyze the meso-scale strain distribution that covers multiple prior austenite grains. The aim is to statistically investigate the points of strain localization before exemplarily focusing on single prior austenite grains at higher resolution. The final results obtained from the ‘field-of-view’ samples (Fig. 2a) are shown as

evolution of local strain distribution in Fig. 3a with the respective local strain maps as insets.¹ The average strain at the deformation steps yields 3.7%, 12.2% and 18.9%. The strain heterogeneity in terms of peak width is gradually increasing indicating strain localization during deformation. Fig. 3b correlates the thresholded local strain map (> 20%) from the second deformation step with the Taylor

¹ Three types of strain measures are relevant in this context: First, we use the ‘local strains’ that are derived from the symmetric portion of the displacement gradient tensor that is locally derived via digital image correlation. Second, we use the ‘average strain’ to describe the global deformation of the wider region of interest that by adding up all the individual strains obtained locally. Third, in some cases one may refer to nominal strains which is the deformation indicated by the machine. For identifying the underlying deformation mechanisms the local strains are particularly relevant.

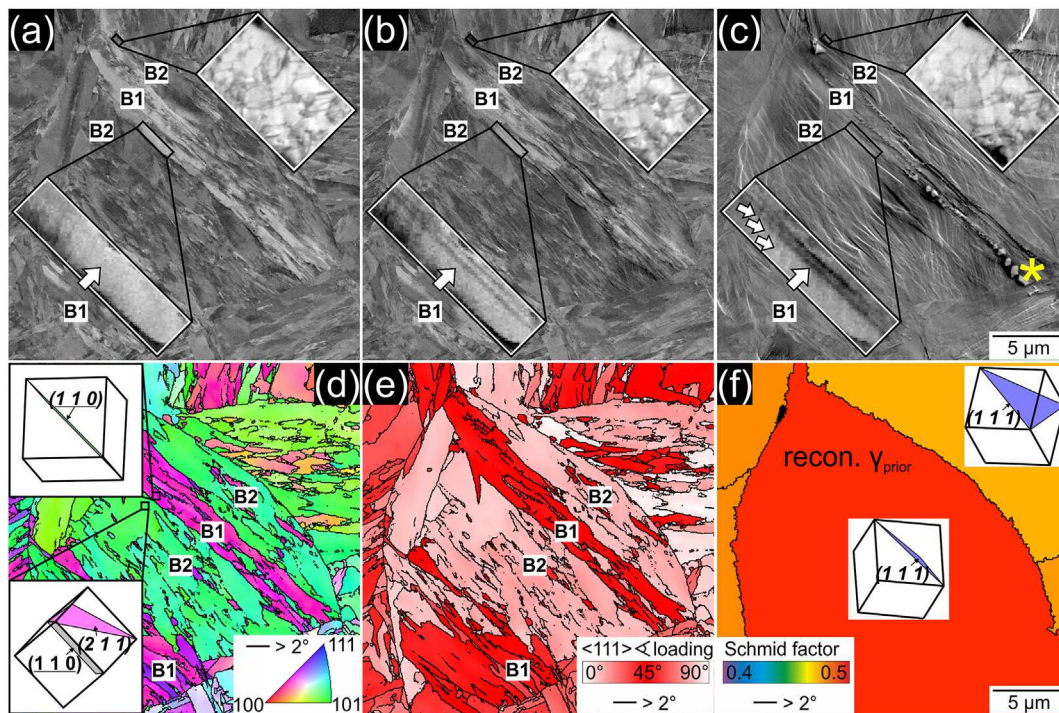


Fig. 6. (a) SE image of the undeformed microstructure with high magnification SE and ECCI (inverted for better visual clarity) insets; (b) and (c) show the deformation response. Contamination artifacts in the highly deformed areas are marked with a yellow star; (d) inverse pole figure map showing the same undeformed microstructure as in (a) with insets illustrating the highest Schmid factor slip systems (purple) and interfacial planes (grey) in two blocks, B1 and B2; (e) color coded map showing angle between $\langle 111 \rangle$ slip direction and horizontal tensile loading axis; (f) Schmid factor map of reconstructed austenite structure with highest Schmid factor slip systems (blue) indicated in two austenite grains. SE: secondary electron; ECCI: electron channeling contrast imaging. (For interpretation of the references to colour in this figure legend, the reader is referred to the web version of this article.)

factor map obtained from EBSD analysis of the initially undeformed microstructure. The Taylor factor serves here as a simplified kinematic homogenization measure that quantifies the total amount of crystallographic shear required for compatible grain deformation per microscopic unit deformation step. The more crystallographic slip is needed (high Taylor factor) the more intense the grain hardness and hardening is supposed to be in this context. This means that Taylor factors are approximate individual grain strength measures and can serve to evaluate the deformation ability of each martensite portion under the applied loading conditions [44]. The overlaying of both, Taylor factor and strain maps requires image distortion that is guided using the etched microstructure images obtained for strain mapping. For full field-of-view quantification, the strain value at every pixel is correlated with the corresponding value of Taylor factor (i.e. both maps are coarsened to the same resolution). Fig. 3c shows the collection of all pixels plotted as Taylor factor against strain value. As the resulting slope of the linear fit is approximately null (0.049), this analysis does not reveal any significant correlation between strain localization zones and the corresponding Taylor factor.

In Fig. 4 we present another EBSD overlay for identifying texture-topology-strain correlations based on the geometric lath alignment. Here, lath alignment refers to the 2D surface-projected orientation of the lath longitudinal direction. In order to automatically determine the lath alignment, the grain tolerance angle is decreased to 2° so that stacks of laths can be separately identified by the TSL OIM software.² Then, the identified grains are fitted with

an ellipsoid shape using the ellipse orientation function in the TSL OIM software. The major axis of the ellipse is assumed as the lath longitudinal direction and color coded with respect to the angle against the tensile direction from 0° to 90° , as exemplarily shown in the cropped region in Fig. 4a. Fig. 4b and c reveal the locations of strain localization by overlaying the thresholded strain map. After 3.7% average strain, strain localization is only observed along $\sim 45^\circ$ oriented laths. After 12.2% average strain, further strain localization along $\sim 45^\circ$ oriented laths occurs, while also laths deviating from the 45° orientation are covered with local strain bands. For example, also the group of laths with almost parallel orientation to the tensile direction is covered by the surrounding strain pattern. However, the direction of individual strain bands remains predominantly in 45° orientation to the tensile direction.

In order to determine the locations of strain accumulation with highest spatial resolution, Fig. 5a shows a high resolution strain map (Fig. 2b) of a zone that includes approximately one prior austenite grain. On top of the strain map the outlines of high angle boundaries with misorientations larger than 12° are overlaid. This misorientation selection includes martensite block and packet boundaries as well as prior austenite grain boundaries [10]. The correspondence between strain localization and high angle boundaries is revealed by recording a strain profile together with a point-to-point misorientation analysis, as shown in Fig. 5b along the red arrow in Fig. 5a. The high angle boundaries are indicated by vertical lines which coincide in every case with a local strain peak. Four of the major six strain peaks correspond to high angle boundaries. This result reveals that significant strain localization is taking place at high angle boundaries. However, strain localization is also observed in the bulk of the blocks (i.e. away from the boundaries) as indicated by the fluctuations in the strain profile. Both of these plastic accommodation processes, (i) in the bulk and (ii) at interfaces, are further studied next by surface trace analysis.

² Usually, low angle lath boundaries ($< 5^\circ$) are not consistently captured by EBSD probing in SEM. However, a stack of laths with almost identical crystallographic orientation, i.e. a sub-block, exhibits the same longitudinal direction as the individual lath components.

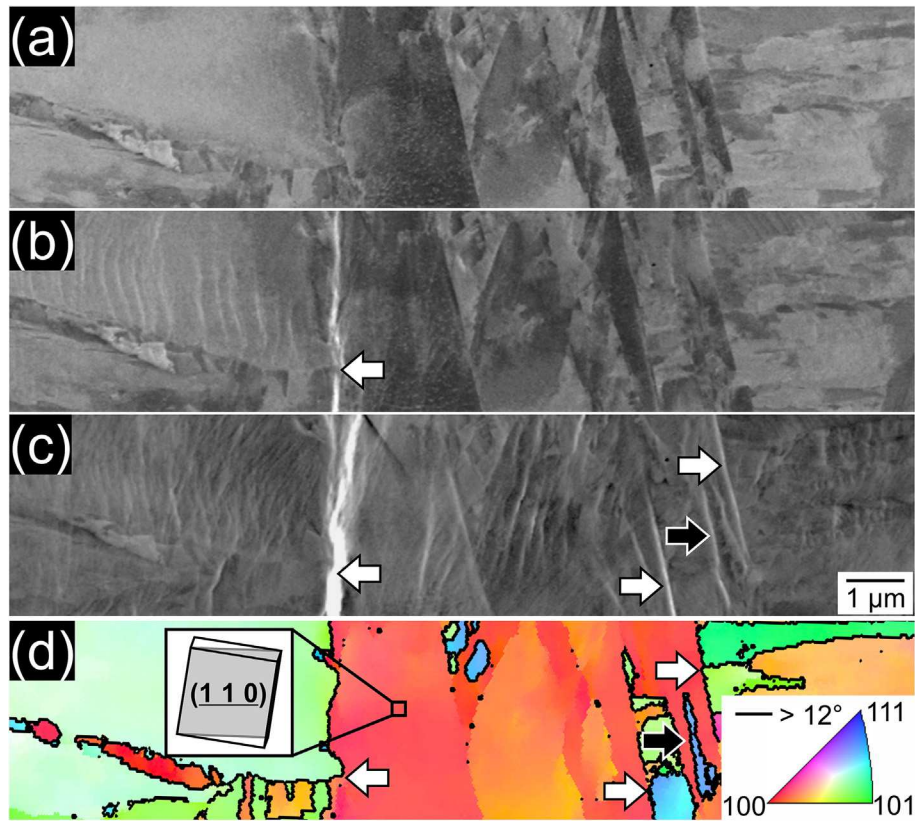


Fig. 7. (a) SE image of the undeformed microstructure; (b) and (c) show boundary steps upon deformation; (d) inverse pole figure map of the same region as in (a) with highlighted high angle packet (white arrow) and block (black arrow) boundaries, inset shows the $\sim 45^\circ$ orientation to loading direction of the interfacial habit plane. SE: secondary electron.

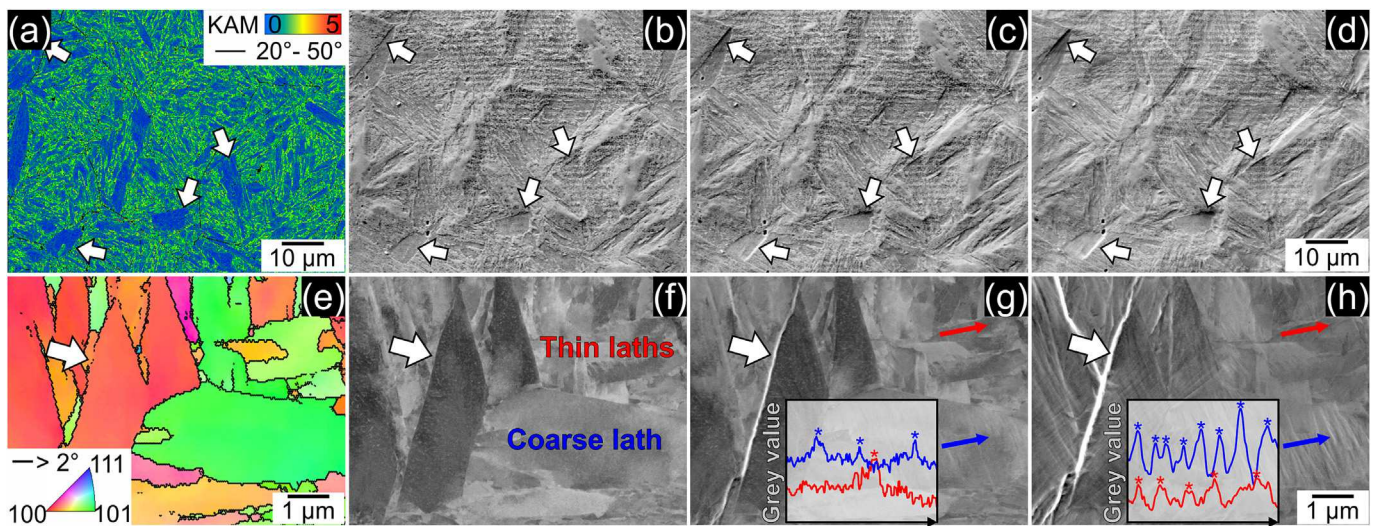


Fig. 8. (a) Kernel average misorientation map of the undeformed microstructure with arrows pointing at typical low-misoriented coarse lath regions; (b) SE image of the same position after slight etching; (c) and (d) deformation response after applying 1.9% and 3.5% nominal strain, respectively. (e) inverse pole figure map of a coarse lath region with arrow pointing at coarse lath boundary; (f) SE image of the same position; (g) and (h) deformation response revealing the appearance of a pronounced boundary step and slip traces; inset in (h) shows grey value profiles in a coarse (blue) and thin (red) lath region with stars marking profile peaks indicative for slip steps. SE: secondary electron. (For interpretation of the references to colour in this figure legend, the reader is referred to the web version of this article.)

3.2. Bulk plasticity

In order to compare bulk and interface plasticity processes, we used SE topographic imaging with residual background diffraction contrast. In this way we image both, the topographic evolution upon deformation and at the same time maintaining the

information about martensitic crystallographic structure. First, we focus on the topography evolution away from martensite boundaries. For this purpose, the tension side of a polished sample was observed in an interrupted 3-point bending experiment. Fig. 6a shows an SE image of mainly one prior austenite grain in the undeformed state. Upon deformation, as shown in Fig. 6b and c, one

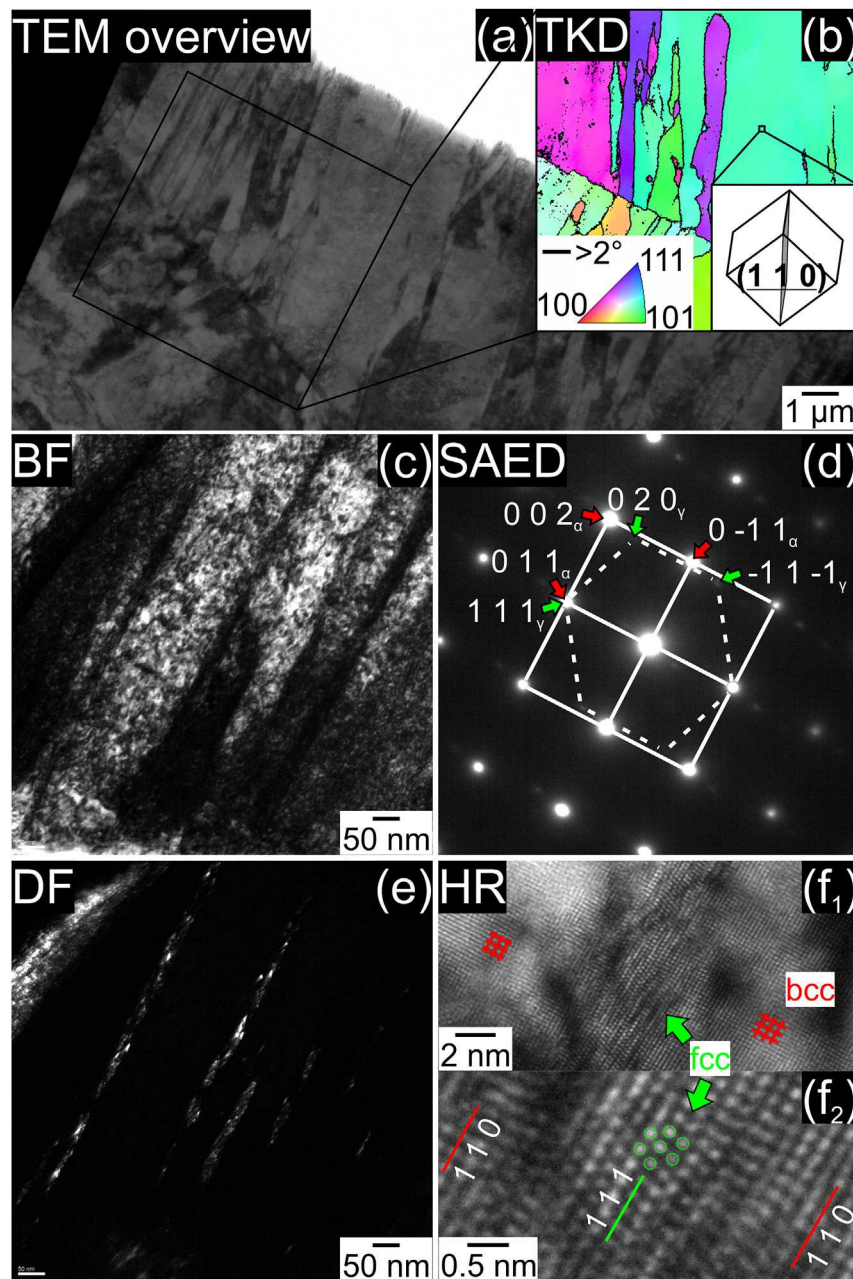


Fig. 9. (a) Bright field TEM overview image of the thin foil specimen with field-of-view inverse pole figure map in (b) revealing the edge-on orientation of laths; (c) bright field TEM image of lath structure with corresponding selected area diffraction pattern in (d) revealing prominent bcc reflections (red) + weak fcc spots (green); (e) dark field TEM image obtained using austenite spot; (f1) high resolution TEM image of same lath boundary as observed in (c); (f2) magnified section showing fcc atomic columns at lath boundary satisfying the K-S orientation relationship. TEM: transmission electron microscopy. (For interpretation of the references to colour in this figure legend, the reader is referred to the web version of this article.)

observes significant plasticity in the middle sections indicated by a high density of steep surface steps in this region. Some of the details of the process are discussed comparatively using the insets in this figure. The top inset shows an ECCI analysis of the interior of a lath neighboring the high deformation region, revealing the dislocation network. The series of ECC images shows no apparent changes to the initial dislocation network structure, despite the imposed deformation. The bottom inset of Fig. 6b, which focuses on the topography evolution in the highly deforming region, shows two surface steps, which lie exactly parallel to the lath longitudinal direction (Fig. 6b). In the second deformation step, shown in Fig. 6c, indications of another set of parallel surface steps, which lie almost perpendicular to the lath longitudinal direction, are revealed.

In Fig. 6d–f the observations discussed above are compared to the EBSD data obtained from the same region in the undeformed state. Fig. 6d shows that the region showing strong localization of plasticity (i.e. including the bottom inset of Fig. 6a–c) corresponds to one specific crystallographic block B1, which is neighbored on both sides by another block B2.³ Apparently, in B1 the slip system with the highest Schmid factor (*italic indices*) is parallel to the

³ Note that there is another B1 block present in the region (bottom left) which shows however less plastic deformation which might be due to the much shorter length in the longitudinal direction and spatial constraints by the prior austenite grain yielding a different strain accommodation response.

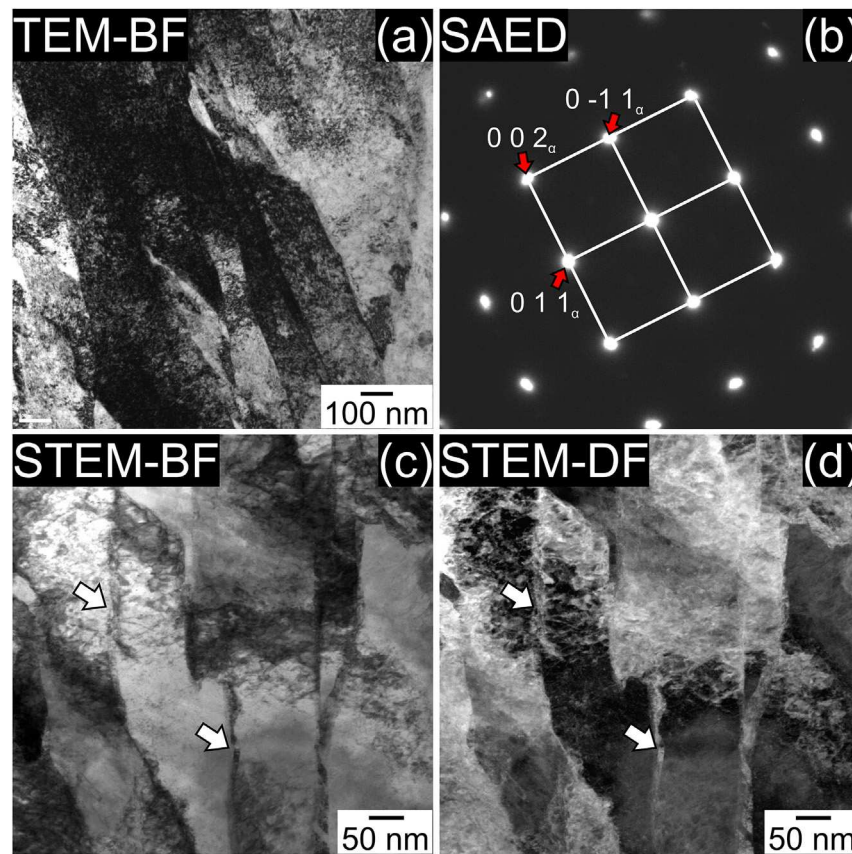


Fig. 10. (a) Bright field TEM image of the deformed microstructure with corresponding selected area diffraction pattern in (b) showing only bcc reflections (red); (c) and (d) scanning-TEM bright field and dark field images revealing disrupted boundary structure. TEM: transmission electron microscopy. (For interpretation of the references to colour in this figure legend, the reader is referred to the web version of this article.)

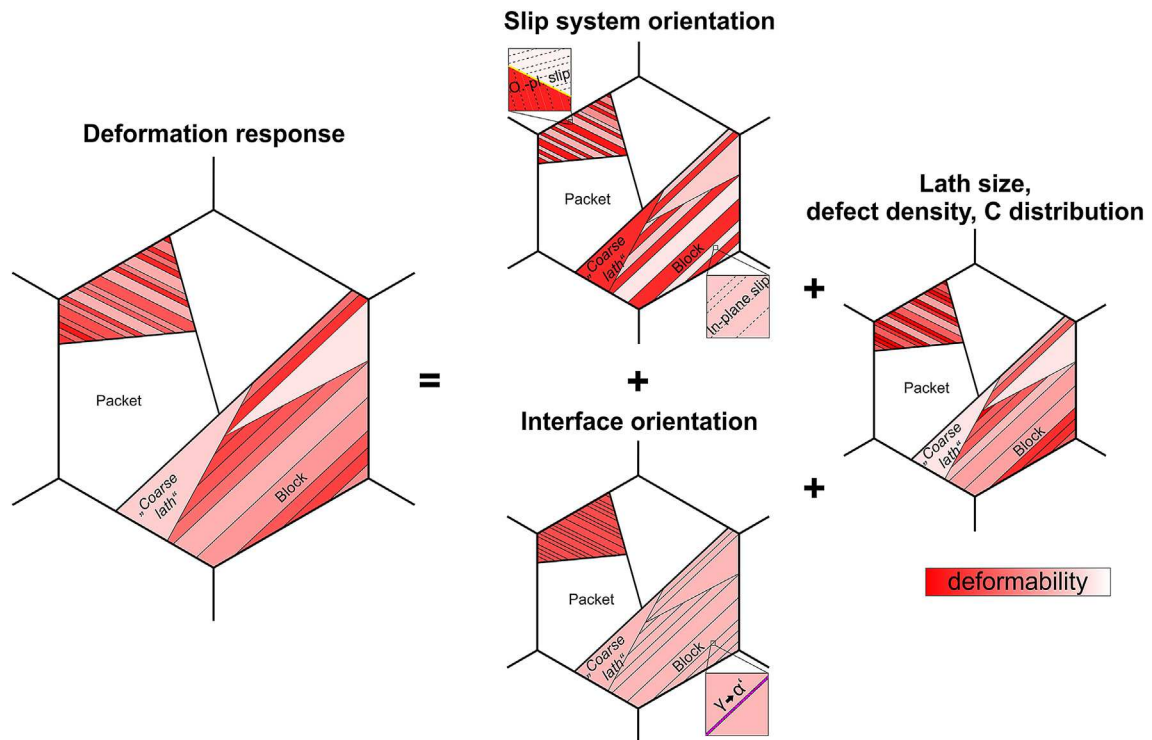


Fig. 11. Schematic representation of deformation mechanisms in lath martensite as a superposition of slip system orientation, interface orientation and initial yield strength distribution due to lath size, defect density and carbon distribution variations (right) to yield the observed deformation response (left).

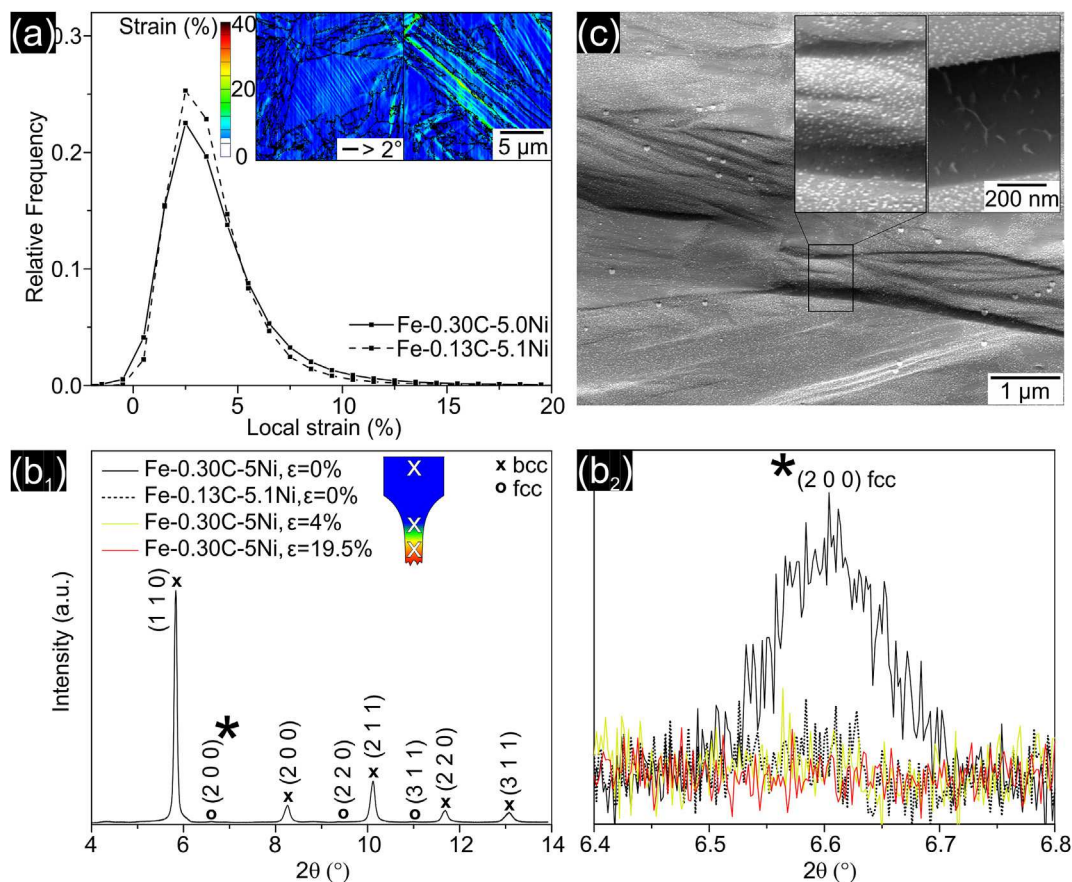


Fig. 12. (a) Comparison of strain distribution in Fe-0.30C-5.0Ni and Fe-0.13C-5.1Ni lath martensite; inset shows strain maps of deformed Fe-0.30C-5.0Ni indicating as well interface and slip plasticity; (b1) s-XRD of Fe-0.30C-5.0Ni revealing bcc peaks; (b2) magnified segment of the fcc peak position with s-XRD profiles overlaid from deformed microstructures and undeformed Fe-0.13C-5.1Ni microstructure; (c) SE image of surface steps on fractured tensile samples revealing boundary steps with indications of embrittlement. s-XRD: synchrotron x-ray diffraction; SE: secondary electron.

interfacial habit plane (underlined indices), as schematically shown in the top inset of Fig. 6d. The primarily observed surface steps in this region coincide with the direction of the slip system plane traces. However in less deformed B2, a {211}<111> slip system has the highest Schmid factor.

To illustrate why different slip systems are activated within the same packet, Fig. 6e shows the orientation of the <111> slip direction with respect to the loading direction. In B1 the best oriented <111> direction is very close to the optimum 45° creating the highest resolved shear stress. In B2, however, the favorable <111> direction is significantly more deviating from 45°, so that another slip system is activated. In Fig. 6f the highest Schmid factor slip systems are analyzed for the reconstructed prior austenite grain structure. The slip system, which would be hypothetically favored in the center prior austenite grain (if the prior austenite would be deformed, instead of the transformed martensite), has a higher Schmid factor than those in the surrounding austenite grains. Also note that the {111} fcc slip plane in the center prior austenite grain is exactly parallel to the {110} slip plane being activated in B1 after martensitic transformation, as it is clear from the respective insets (Fig. 6d and f).

3.3. Interface plasticity

In Fig. 7 another region from the tensile part of the 3-point bending sample is analyzed. Fig. 7a shows an SE image in the undeformed state. Note that in the middle part of the investigated area the lath long directions are near-perpendicular, while on both

sides they are near-parallel, with respect to the loading direction. Following the first deformation step (Fig. 7b), a steep surface step appears right at the boundary between horizontally and vertically aligned laths. Upon further deformation (Fig. 7c), this step gets even more pronounced, while at the other side three surface steps develop at other martensite boundaries. The crystallographic orientations in the observed region are shown in Fig. 7d by an inverse pole figure map with arrows pointing at the positions of boundary surface steps. The group of vertical laths is surrounded by two packet boundaries (i.e. revealed by the change of geometric lath orientation) marked with white arrows. Importantly, both packet boundaries correspond to locations of boundary surface steps. It becomes obvious that a different deformation process must be activated that is limited only to the interfacial regions, which is in clear contrast to the appearance of slip traces away from boundaries in the bulk martensite, as shown in Fig. 6. Also, within the center packet in Fig. 7, a slightly weaker surface step appears right at a block boundary, as indicated by the black arrow. EBSD analysis further reveals that the orientation of the interfacial plane in the middle packet is oriented about 43° to the loading direction, as indicated by the inset in Fig. 7d.

3.4. Influence of microstructure heterogeneity

The bulk and interface plasticity mechanisms discussed above are influenced by lath size variations in the as-quenched microstructure. Fig. 8a presents a large field-of-view kernel average misorientation map (analyzed within first nearest neighbourhood

of EBSD data points) of the undeformed microstructure. Typical coarse lath regions, as they were introduced in Ref. [15], are marked with arrows. Fig. 8b–d shows the microstructural evolution upon deformation applied as fully in-situ tensile loading in the horizontal direction. The undeformed microstructure is shown in Fig. 8b with arrows pointing at the same coarse laths.

The topographic evolution upon deformation to 1.9% (Fig. 8c) and 3.5% nominal strain (Fig. 8d) indicates surface steps especially at coarse lath boundaries. The surface steps are identified by contrast changes. Fig. 8e and f zoom-in to a coarse lath region from the 3-point bending experiment, providing corresponding inverse pole figure map and topographic SE images. The entire area constitutes a single crystallographic packet. The evolution of surface steps upon deformation is shown in Fig. 8g and h, revealing a distinct surface step at the coarse lath boundary marked with an arrow. Note that the crystallographic orientation of the coarse lath coincides with the one in the inset in Fig. 7d exhibiting $\sim 45^\circ$ orientation of the interface with respect to the tensile direction. Apart from the localization of plasticity at this coarse lath boundary, also the coarse lath interiors show pronounced slip activity. This is obvious from the appearance of regular step patterns starting at the first deformation step (Fig. 8g), while in the surrounding thin laths almost no slip steps are present. The densities of slip traces is quantified by plotting the grey value profile in a coarse and in a thin lath region of almost same crystallographic orientation along the arrows shown in Fig. 8g and h.⁴ In the first deformation step three slip traces appeared along the blue arrow (coarse lath) and only one slip trace in the thin lath indicating that slip plasticity is initiated in the coarse lath region. In the second deformation step the coarse laths are covered with a dense pattern of steps, while significantly less slip activity is observed in the neighboring thin laths, as it is obvious from the inset of Fig. 8h.

3.5. Role of thin austenite films

In order to investigate the origin of the observed interface plasticity, post-mortem TEM analysis is carried out on thin film samples lifted-out after completed deformation tests with strain mapping. TEM samples are prepared from four different regions in the strain map shown in Fig. 2a2 with different local strain levels. Also, an undeformed sample is prepared for TEM investigations. Fig. 9a shows an overview TEM bright field image of the FIB-prepared thin foil lamella from the undeformed microstructure.

Orientation mapping by transmission Kikuchi diffraction reveals that in the top part of the lamella laths are oriented with interfaces perpendicular to the specimen plane, as shown by the $\{110\}$ interfacial plane orientation in Fig. 9b. This configuration is desirable for the detection of thin film austenite, since diffraction overlap can be avoided. Fig. 9c shows the typical undeformed martensite lath structure with TEM bright field imaging. The diffraction pattern shown in Fig. 9b reveals the homogeneous $\langle 100 \rangle$ zone axis orientation of martensite indicating that no high angle boundaries are present in the selected area of Fig. 9a. Still, in addition, weak reflections forming a distorted hexagonal pattern and corresponding to an fcc phase are observed. As revealed by the dark field image from the $(-11-1)$ austenite spot, the fcc phase is located at the martensite interfaces which is in good agreement with previous TEM studies on thin film retained austenite [32–34]. One set of $\{110\}$ martensite and $\{111\}$ austenite spots are on top of each other, thereby fulfilling the K-S orientation relationship

between martensite and austenite. The same lath boundary was investigated by high resolution TEM in the thin edge part of the sample. Fig. 9f shows the $\langle 100 \rangle$ oriented martensite matrix on both sides of the boundary and the atomic arrangements in the interfacial region by means of high resolution TEM. The Fourier transformation signal from the boundary region (not shown here) well corresponds to the observed diffraction pattern in Fig. 9b indicating the presence of an fcc phase. In fact, the hexagonal distorted pattern is present in the high resolution image indicated by green marks on the $\{111\}$ austenite lattice planes. The red lines show the $\{110\}$ martensite planes where the $\{110\}$ habit plane is also parallel to one $\{111\}$ fcc plane.

The deformed microstructure is shown in Fig. 10a in terms of bright field TEM, as one example of the four specimens investigated. The sample was tilted again to the $\langle 100 \rangle$ zone axis as shown by the diffraction pattern in Fig. 10b, however now lacking the presence of austenite spots. The disappearance of fcc spots is confirmed by diffraction patterns of the same orientation in the other three TEM samples, with varying local strain levels around the average value of 18.9% (see Fig. 2d2). Instead, the STEM-bright field and –dark field images in Fig. 10c and d indicate a roughened lath boundary structure after deformation which is in good agreement with TEM observations by Morito et al. [39]. The contrast changes along the interface are marked with white arrows.

4. Discussion

These results suggest that for an improved understanding of lath martensite plasticity a simplified view that considers only crystallography - neglecting microstructure morphology and interface density - is not sufficient (see Figs. 3–5). In fact, these microstructural factors have superimposing effects on bulk and interface plasticity mechanisms. For the former, the activation of the in-lath-plane slip system enables enhanced local plasticity due to the long dislocation mean free path in the lath's longitudinal direction [45]. The example in Fig. 6 shows that the initial plasticity in the observed prior austenite grain is mostly carried by the center block, where in-lath-plane slip is initiated in contrast to the less deformed surrounding blocks. This observation is in good agreement with previous studies analyzing the peculiarities of in-lath-plane slip in lath martensite [25,29–31]. It is widely confirmed that slip deformation is initiated by the activation of in-lath-plane slip.

Considering this special slip mechanism in lath martensite, it is important to note that in a given packet the geometric lath orientation remains the same. Thus, also the in-lath slip plane is parallel with the same resolved shear stress under constant loading conditions. However, it is the slip direction that differs among blocks in one packet and decides whether the in-lath- or any out-of-lath-plane slip system is activated. In the example presented in Fig. 6 it is in fact the most favorable $\{110\}\langle 111 \rangle$ slip system (i.e. with the highest Schmid factor) that is activated in the center block. This becomes clear from the Schmid factor analysis of the prior austenite grain orientation. Since the $\{111\}\langle 110 \rangle$ austenite slip systems are parallel to the $\{110\}\langle 111 \rangle$ martensite slip systems under the K-S orientation relationship, the highest Schmid factor austenite slip system correlates with its martensite counterpart (see Fig. 6d and e). The prior austenite grain structure already determines the orientation of, in particular, the in-lath-plane slip systems in martensite. Assuming that all variants are equally present in one prior austenite grain [46], the austenite grain with the highest Schmid factor might also initiate plasticity earliest in the deformation process, though the austenite grains transformed to martensite. Hence, the investigated grain in Fig. 6 is capable of carrying the initial plasticity (see Fig. 5e).

Naturally, the slip system orientations are one of the factors that

⁴ Slip steps are indicated by bright lines appearing from the topographic effect on the SE signal. The difference in base grey value is due to the slight orientation differences yielding another background diffraction contrast.

determine the observed strain localization and deformation behavior. Fig. 11 shows schematically how the observed deformation response is a superposition of different factors. Interestingly, it was observed that besides slip plasticity inside the laths, also significant plasticity is taking place right at the boundaries, which is in excellent agreement with recent results of Du et al. [38]. Our results show that the strain localizes especially at high angle block and packet boundaries (see Fig. 5). At block boundaries the geometric lath orientation is maintained, however, the crystallographic orientation is changing resulting in a mismatch among the slip systems that are active on adjacent sides of the interface, resulting in local strain incompatibility [47,48]. Thus, high stress localization due to piling-up of dislocations is expected on the boundary plane resulting in the observed boundary surface steps, e.g. in Fig. 7.

Also, packet boundaries are prone to experience strain localization. At packet boundaries the geometric lath orientation is changed, i.e. martensite is transformed on another habit plane. In fact, packet boundaries are asymmetric, since laths on one side (which formed earlier in the sequence of martensitic transformation) lie parallel to the packet boundary, while on the other side laths end with their short edges at the packet boundary. This effect adds to the crystallographic misorientation of $\sim 40^\circ$ – 60° that also exists across packet boundaries [11]. In general, the resolved shear stress on the interfacial plane is highest, if the plane is oriented in 45° to the local loading direction. In fact, the pronounced surface step observed at the packet boundary in Fig. 7a–c is in very good agreement with the near 45° orientation of the interfacial plane. This condition is fulfilled for all laths in this packet and hence also these surface steps appeared at other positions. This observation is fully supported by the results from micro-tensile experiments by Du et al. probing specific boundary arrangements with respect to the loading direction, where most pronounced boundary sliding was observed for tilted boundaries with high resolved shear stresses [38]. Thus, the topological inclination of the interface plane is another factor, besides the slip system orientation, which contributes to the experimentally observed deformation response via interface plasticity. Hence, this effect is included in Fig. 11. In fact, both, the interface plasticity and slip initiation in the lath bulk are facilitated by a near 45° oriented {110} habit plane with respect to the loading direction. Yet, it remains challenging to evaluate the relative contributions of both mechanisms to the overall deformation response. Du et al. concluded that, in case of preferential interface orientation, interface plasticity dominates over crystallographic slip [38]. Thus, the initial deformation might be carried by interface and in-lath-plane plasticity, which is supported by our strain localization results showing early localization along the lath longitudinal directions (see Fig. 4). The later arising strain incompatibilities are then accommodated by transgranular slip, as it is for example visible in Fig. 7 for the laths with interfaces parallel to the loading direction showing perpendicular slip traces, e.g. in contrast to the favorable oriented center laths. Returning to the strain histograms in Fig. 3, the strain distribution at a given deformation step can be interpreted as the overlap of a sharp strain localization component (caused by interface plasticity) and a more broad, diffuse strain localization component caused by crystallographic slip. The fact that no peak separation is observed at any step might hint at both mechanisms being equally activated during deformation.

Another group of interfaces in the lath martensitic microstructure are prior austenite grain boundaries [11,49]. In contrast to packet, block and sub-block boundaries, the character of prior austenite grain boundaries is not determined by the austenite-martensite orientation relationship. Also, the boundary plane is curved, while martensite boundaries are typically straight due to the strict orientation relationship and the minimization of

accommodation strain energy during martensitic transformation. As no specific strain localization was observed at prior austenite grain boundaries, it might be concluded that flat interfaces are favored for interface plasticity.

Both, slip plasticity and interface plasticity are altered by the initially heterogeneous lath martensitic microstructure after quenching. This was exemplarily shown with the deformation behavior of typical coarse lath regions. Coarse laths were characterized as less dislocated, significantly extended in size, highly autotempered and thereby softer than the surroundings, since they form earliest in the course of martensitic transformation [15]. In the area shown in Fig. 8, coarse and thin laths coexist with the same orientations of two crystallographic blocks. Still, plasticity is initiated in the coarse lath regions. This is in good agreement with the fact that coarse laths represent soft spots in the microstructure and therefore plastically yield earliest, leading to early appearance of slip steps (see Fig. 8b). Further, coarse lath boundaries are especially prone to interface plasticity. As coarse laths lack any internal boundaries, it becomes clear that the incompatibilities with the surrounding microstructure need to be accommodated by only a few boundaries compared to a typical parallel arrangement of thin laths, where the strain can be partitioned to multiple boundaries. In general, it can be concluded that both, bulk and interface plasticity are enhanced in coarse laths. Or, in other words, the deformability is increasing from late (less autotempered, highly dislocated) to early (highly autotempered, less dislocated) martensite. Thus, the variations in lath size, defect density and autotempering state induced by the martensitic transformation sequence are included in Fig. 11 as the third factor affecting the deformation response of lath martensite.

Having all identified factors collected in Fig. 11, it now becomes possible to discuss and qualitatively predict the deformation response of a given martensitic microstructure. These guidelines are applicable for example to the analysis of lath martensite deformation with crystallographical and morphological differences inherited by transformation from ultra-fine grained [50] and hot-deformed austenite [51], which will be the focus of our future work. Yet, the nano-scale mechanisms enabling the observed interface plasticity remain mostly unclear so far. It was shown here that thin film austenite exists in the as-quenched microstructure (see Fig. 9), which is stabilized and retained by carbon segregation to martensite boundaries as an autotempering reaction during quenching [52–56]. Since the retained austenite satisfies the K-S orientation relationship with the surrounding martensite, intrinsically {111}<110> fcc slip systems lie parallel within the interfacial plane. It was shown by crystal plasticity modelling that by considering martensite as a two phase microstructure even with only a small fraction of inter-lath austenite, the mechanical behavior can be well reproduced [35,36,57]. However, our TEM investigations indicate the disappearance of the thin film austenite upon loading, indicating its gradual deformation-driven transformation into fresh martensite. Hence, the austenitic phase could only carry plasticity during the earliest stages of deformation, but not to a large extent and, most importantly, not throughout the entire deformation process.

For a second confirmation of the transformation of austenite, the deformation process of an alloy with higher carbon content, namely Fe-0.30C-5Ni, was investigated. By increasing the carbon content to 0.30 wt% a larger fraction of thin film austenite can be retained [58,59]. This alloy was deformed in the same way as the Fe-0.13C-5.1Ni alloy presented in Fig. 2a with strain mapping analysis correlated with EBSD crystallographic mapping. Fig. 12a shows the strain distribution histogram after an average straining of 3.9% which is compared to the Fe-0.13C-5.1Ni counterpart with an average strain of 3.7%. In both cases, almost the same strain

distribution is observed indicating that the same deformation mechanisms are activated. This is confirmed by the strain maps with martensite boundaries overlaid from EBSD analysis shown in the insets of Fig. 12a. Same as in the low-carbon alloy, slip traces are resolved in a coarse lath region (inset 1), as well as pronounced strain localization along the lath longitudinal direction presumably at interfaces (inset 2). Fig. 12b1 shows an s-XRD pattern obtained at the undeformed state of Fe-0.30%–5Ni. Besides the major peaks corresponding to the bcc-Fe martensitic matrix, weak, but clearly identified peaks corresponding to (200), (220) and (311) fcc peaks are observed. The (111) fcc peak is overlapping with the high intensity (110) bcc peak. Fig. 12b2 shows a magnified segment of the diffraction pattern including only the (200) fcc peak. The calculated lattice spacing from the 2 θ peak position yields 0.179 nm and well corresponds to the (200) lattice spacing from the TEM diffraction pattern (see Fig. 8a2). In order to analyze the phase compositions with respect to different levels of deformation, a post-mortem s-XRD investigation is carried out on a fractured tensile sample. Along the tensile axis, the strain gradient is known from optical DIC analysis based on spray coating. The strain profile together with the respective synchrotron measurement positions are illustrated in the inset of Fig. 12b1. In Fig. 12b2 these s-XRD patterns are overlaid to the undeformed curve focusing on the (200) fcc peak position. Already at 4% average strain the austenite peak disappeared. The disappearance of the austenite peaks is confirmed by patterns from higher local strain levels all lacking any austenite peaks, also in the (220) and (311) fcc peak positions. As a reference, also the s-XRD pattern of undeformed Fe-0.13C–5.1Ni is shown which only shows a slight indication of the (200) austenite peak with significantly lower intensity. Thus, the austenite volume fraction in Fe-0.13C–5.1Ni might be even below 1% which is in agreement with our high resolution TEM analysis.

Another Fe-0.30C–5Ni fractured tensile sample was used for detailed observation of the steps created on the as-prepared surface after deformation. Therefore, in SEM, the sample was tilted to 70° and rotated about 45° with respect to the loading axis to see on top of some surface steps that appeared in 45° orientation to the loading direction. The left inset in Fig. 12c shows a magnified image of one surface step. The creation of the surface step during deformation is confirmed by the absence of the dense SiO₂ particle pattern, which was originally applied on the sample surface to measure the local strain. To clarify the local surface structure caused by the interface plasticity, another pronounced surface step is shown in the other inset. Brittle features resembling those found on regular fracture surfaces are suggesting a sort of boundary embrittlement. Since the thin film austenite is enriched with carbon that has been expelled from the supersaturated bcc lattice during quenching, high-carbon martensite films are supposed to be present at the boundaries after slight nominal deformation of e.g. 10% cold rolling [60]. As a consequence, one possibility is that dislocation motion is hindered across boundaries, thereby, creating high stresses on the interface. Surprisingly, only very rarely decohesion resulting in μ -cracks was observed until the final stages before fracture. Importantly, Ohmura et al. observed a difference in dislocation transmission across high-angle and low-angle boundaries in Fe–C martensite by in-situ nanoindentation [40]. At low-angle lath boundaries dislocation motion was hindered by dense arrays of dislocations at the lath boundary, so that a critical stress was required to transmit a diffuse dislocation cloud into the adjacent grain. However, at a high-angle block boundary Ohmura et al. surprisingly found that dislocations are simply transferred and absorbed in the grain boundary plane which is accomplished by so-called boundary sliding on the {110} interfacial planes. On the block boundary plane two adjacent martensite variants share the same {110}<111> slip systems, thereby enabling dislocation gliding along

the interface. This results in the typical shearing motion of two adjacent martensite blocks with however rather limited deformation of the respective martensite bulks. In fact, this observation is in very good agreement with our results on prominent plasticity localization right at high-angle block and packet boundaries, so that the process suggested by Ohmura et al. provides the best explanation so far for the occurrence of pronounced interface plasticity in lath martensite.

5. Conclusions

We investigated the deformation behavior of as-quenched Fe-5.1Ni-0.13C and Fe-5.0Ni-0.30C model lath martensitic steels focusing on the role of martensite interfaces, lath topology, crystallography and the presence of thin film retained austenite besides conventional slip plasticity. The deformation response can be described as a superposition of multiple deformation mechanisms:

- Upon deformation, strain localization appears in the bulk of martensite blocks, but notably also at high angle block and packet boundaries in the form of interface plasticity.
- The bulk martensite is deformed by dislocation gliding, where the possible activation of the in-lath-plane slip system enables a locally enhanced plastic response.
- For the occurrence of interface plasticity, the orientation of the boundary plane with respect to the loading direction is the crucial factor. High shear stresses for near 45° orientations enable most pronounced interface plasticity.
- Nano-scale thin film inter-lath austenite is present before deformation, but transformed even before reaching ~4% average strain level and thus might not contribute effectively to the overall plastic process. Instead, dislocation gliding within the {110} interfacial planes supposedly enables the observed sliding motion of adjacent martensite blocks along the interface.
- Both, interface and slip plasticity are altered by the initial yield strength distribution in the as-quenched microstructure induced by lath size, defect density and autotempering variations occurring due to the transformation sequence (i.e. coarse ‘soft’ laths forming just below M_s and fine ‘hard’ laths formed around M_f)

Acknowledgement

The authors gratefully acknowledge the funding by the EU Research Fund for Coal & Steel (RFSR-CT-2013-00013) for the ToolMart project. We also would like to especially thank Prof. Kaneaki Tsuzaki and assist. Prof. Motomichi Koyama, as well as the Japan Society for Promotion of Science for enabling and granting a fruitful research visit to Kyushu University. Jean-Louis Collet from CRM also kindly contributed to this work by acquiring the s-XRD data. Preliminary TEM analyses were supported by Sebastian Cobo, Ian Zuazo and Patrick Barges from ArcelorMittal Maizières Research SA.

References

- [1] E.I. Galindo-Nava, P.E.J. Rivera-Díaz-del-Castillo, Understanding the factors controlling the hardness in martensitic steels, *Scr. Mater.* 110 (2016) 96–100.
- [2] M.M. Wang, C.C. Tasan, D. Ponge, A.C. Dippel, D. Raabe, Nanolaminate transformation-induced plasticity-twinning-induced plasticity steel with dynamic strain partitioning and enhanced damage resistance, *Acta Mater.* 85 (2015) 216–228.
- [3] M.M. Wang, C.C. Tasan, D. Ponge, A. Kostka, D. Raabe, Smaller is less stable: size effects on twinning vs. transformation of reverted austenite in TRIP-maraging steels, *Acta Mater.* 79 (2014) 268–281.
- [4] B. Hutchinson, J. Hagström, O. Karlsson, D. Lindell, M. Tornberg, F. Lindberg, M. Thuvander, Microstructures and hardness of as-quenched martensites

- (0.1–0.5%), *Acta Mater.* 59 (2011) 5845–5858.
- [5] G. Krauss, Martensite in steel: strength and structure, *Mat. Sci. Eng. A Struct.* 273 (1999) 40–57.
 - [6] D. Kalish, M. Cohen, Structural changes and strengthening in the strain tempering of martensite, *Mater. Sci. Eng.* 6 (1970) 156–166.
 - [7] E.I. Galindo-Nava, P.E.J. Rivera-Díaz-del-Castillo, A model for the microstructure behaviour and strength evolution in lath martensite, *Acta Mater.* 98 (2015) 81–93.
 - [8] S.C. Kennett, G. Krauss, K.O. Findley, Prior austenite grain size and tempering effects on the dislocation density of low-C Nb–Ti microalloyed lath martensite, *Scr. Mater.* 107 (2015) 123–126.
 - [9] G. Krauss, Deformation and fracture in martensitic carbon steels tempered at low temperatures, *Metall. Mater. Trans. B* 32 (2001) 205–221.
 - [10] S. Morito, X. Huang, T. Furuhara, T. Maki, N. Hansen, The morphology and crystallography of lath martensite in alloy steels, *Acta Mater.* 54 (2006) 5323–5331.
 - [11] S. Morito, H. Tanaka, R. Konishi, T. Furuhara, T. Maki, The morphology and crystallography of lath martensite in Fe–C alloys, *Acta Mater.* 51 (2003) 1789–1799.
 - [12] H. Kitahara, R. Ueji, N. Tsuji, Y. Minamino, Crystallographic features of lath martensite in low-carbon steel, *Acta Mater.* 54 (2006) 1279–1288.
 - [13] G. Kurdjumov, Phenomena Occurring in the Quenching and Tempering of Steels, Institute of Materials, 1 Carlton House Terrace, London, SW 1 Y 5 DB, UK, 2001, pp. 117–162.
 - [14] C.C. Kinney, K.R. Pytlewski, A.G. Khachatryan, J.W. Morris, The microstructure of lath martensite in quenched 9Ni steel, *Acta Mater.* 69 (2014) 372–385.
 - [15] L. Morsdorf, C.C. Tasan, D. Ponge, D. Raabe, 3D structural and atomic-scale analysis of lath martensite: effect of the transformation sequence, *Acta Mater.* 95 (2015) 366–377.
 - [16] J.-I. Zhang, L. Morsdorf, C.C. Tasan, D. Raabe, Quasi In-situ Methodology for Tracking Microstructural Evolution in Complex Microstructures during Thermo-processing, 2015.
 - [17] M.K. Miller, P.A. Beaven, G.D.W. Smith, A study of the early stages of tempering of iron-carbon martensites by atom probe field-ion microscopy, *Metall. Trans. A* 12 (1981) 1197–1204.
 - [18] G. Badinier, C.W. Sinclair, X. Sauvage, X. Wang, V. Bylik, M. Gouné, F. Danoix, Microstructural heterogeneity and its relationship to the strength of martensite, *Mater. Sci. Eng. A* 638 (2015) 329–339.
 - [19] S. Allain, O. Bouaziz, M. Takahashi, Toward a new interpretation of the mechanical behaviour of as-quenched low alloyed martensitic steels, *ISIJ Int.* 52 (2012) 717–722.
 - [20] S. Takaki, K.-L. Ngo-Huynh, N. Nakada, T. Tsuchiyama, Strengthening mechanism in ultra low carbon martensitic steel, *ISIJ Int.* 52 (2012) 710–716.
 - [21] J. Wilde, A. Cerezo, G.D.W. Smith, Three-dimensional atomic-scale mapping of a Cottrell atmosphere around a dislocation in iron, *Scr. Mater.* 43 (2000) 39–48.
 - [22] T. Ohmura, T. Hara, K. Tsuzaki, Evaluation of temper softening behavior of Fe–C binary martensitic steels by nanoindentation, *Scr. Mater.* 49 (2003) 1157–1162.
 - [23] J.W. Morris Jr., M. Jin, A.M. Minor, In situ studies of the transmission of strain across grain boundaries, *Mater. Sci. Eng. A* 462 (2007) 412–417.
 - [24] S. Morito, H. Yoshida, T. Maki, X. Huang, Effect of block size on the strength of lath martensite in low carbon steels, *Mater. Sci. Eng. A* 438–440 (2006) 237–240.
 - [25] A. Shibata, T. Nagoshi, M. Sone, S. Morito, Y. Higo, Evaluation of the block boundary and sub-block boundary strengths of ferrous lath martensite using a micro-bending test, *Mater. Sci. Eng. A* 527 (2010) 7538–7544.
 - [26] H. Ghassemi-Armaki, P. Chen, S. Bhat, S. Sadagopan, S. Kumar, A. Bower, Microscale-calibrated modeling of the deformation response of low-carbon martensite, *Acta Mater.* 61 (2013) 3640–3652.
 - [27] C. Du, J.P.M. Hoefnagels, R. Vaes, M.G.D. Geers, Block and sub-block boundary strengthening in lath martensite, *Scr. Mater.* 116 (2016) 117–121.
 - [28] D. Raabe, Simulation of rolling textures of b.c.c. metals considering grain interactions and crystallographic slip on {110}, {112} and {123} planes, *Mater. Sci. Eng. A* 197 (1995) 31–37.
 - [29] M. Michiuchi, S. Nambu, Y. Ishimoto, J. Inoue, T. Koseki, Relationship between local deformation behavior and crystallographic features of as-quenched lath martensite during uniaxial tensile deformation, *Acta Mater.* 57 (2009) 5283–5291.
 - [30] S. Nambu, M. Michiuchi, Y. Ishimoto, K. Asakura, J. Inoue, T. Koseki, Transition in deformation behavior of martensitic steel during large deformation under uniaxial tensile loading, *Scr. Mater.* 60 (2009) 221–224.
 - [31] Y. Mine, K. Hirashita, H. Takashima, M. Matsuda, K. Takashima, Micro-tension behaviour of lath martensite structures of carbon steel, *Mater. Sci. Eng. A* 560 (2013) 535–544.
 - [32] S. Morito, K. Oh-ishi, K. Hono, T. Ohba, Carbon enrichment in retained austenite films in low carbon lath martensite steel, *ISIJ Int.* 51 (2011) 1200–1202.
 - [33] F.H. Samuel, Effect of dual-phase treatment and tempering on the microstructure and mechanical properties of a high strength, low alloy steel, *Mater. Sci. Eng.* 75 (1985) 51–66.
 - [34] D.H. Sherman, S.M. Cross, S. Kim, F. Grandjean, G.J. Long, M.K. Miller, Characterization of the carbon and retained austenite distributions in martensitic medium carbon, high silicon steel, *Metall. Mater. Trans. A* 38 (2007) 1698–1711.
 - [35] F. Maresca, V.G. Kouznetsova, M.G.D. Geers, On the role of interlath retained austenite in the deformation of lath martensite, *Model. Simul. Mater. Sci. Eng.* 22 (2014) 045011.
 - [36] F. Maresca, V.G. Kouznetsova, M.G.D. Geers, Subgrain lath martensite mechanisms: a numerical-experimental analysis, *J. Mech. Phys. Solids* 73 (2014) 69–83.
 - [37] J. Cui, Y.S. Chu, O.O. Famodu, Y. Furuya, J. Hattrick-Simpers, R.D. James, A. Ludwig, S. Thienhaus, M. Wuttig, Z. Zhang, I. Takeuchi, Combinatorial search of thermoelastic shape-memory alloys with extremely small hysteresis width, *Nat. Mater.* 5 (2006) 286–290.
 - [38] C. Du, J.P.M. Hoefnagels, R. Vaes, M.G.D. Geers, Plasticity of lath martensite by sliding of substructure boundaries, *Scr. Mater.* 120 (2016) 37–40.
 - [39] S. Morito, T. Ohba, T. Maki, Comparison of deformation structure of lath martensite in low carbon and ultra-low carbon steels, *Mater. Sci. Forum* 558–559 (2007) 933–938.
 - [40] T. Ohmura, A.M. Minor, E.A. Stach, J.W. Morris, Dislocation-grain boundary interactions in martensitic steel observed through in situ nanoindentation in a transmission electron microscope, *J. Mater. Res.* 19 (2011) 3626–3632.
 - [41] D. Yan, C.C. Tasan, D. Raabe, High resolution in situ mapping of microstrain and microstructure evolution reveals damage resistance criteria in dual phase steels, *Acta Mater.* 96 (2015) 399–409.
 - [42] C. Cayron, ARPGE: a computer program to automatically reconstruct the parent grains from electron backscatter diffraction data, *J. Appl. Crystallogr.* 40 (2007) 1183–1188.
 - [43] D. Mercier, C. Zambaldi, T.R. Bieler, A Matlab toolbox to analyze slip transfer through grain boundaries, *IOP Conf. Ser. Mater. Sci. Eng.* 82 (2015) 012090.
 - [44] G.I. Taylor, Plastic strain in metals, *J. Inst. Met.* 62 (1938) 307–324.
 - [45] Y. Ishimoto, M. Michiuchi, S. Nambu, K. Asakura, J. Inoue, T. Koseki, Measurement of strain distribution of lath martensite microstructure during tensile deformation, *J. Jpn. Inst. Met.* 73 (2009) 720–727.
 - [46] L. Qi, A.G. Khachatryan, J.W. Morris Jr., The microstructure of dislocated martensitic steel: Theory, *Acta Mater.* 76 (2014) 23–39.
 - [47] T.R. Bieler, P. Eisenlohr, F. Roters, D. Kumar, D.E. Mason, M.A. Crimp, D. Raabe, The role of heterogeneous deformation on damage nucleation at grain boundaries in single phase metals, *Int. J. Plast.* 25 (2009) 1655–1683.
 - [48] F. Roters, P. Eisenlohr, L. Hantcherli, D.D. Tjahjanto, T.R. Bieler, D. Raabe, Overview of constitutive laws, kinematics, homogenization and multiscale methods in crystal plasticity finite-element modeling: theory, experiments, applications, *Acta Mater.* 58 (2010) 1152–1211.
 - [49] N. Nakada, R. Fukagawa, T. Tsuchiyama, S. Takaki, D. Ponge, D. Raabe, Inheritance of dislocations and crystallographic texture during martensitic reversion into austenite, *ISIJ Int.* 53 (2013) 1286–1288.
 - [50] T. Furuhara, K. Kikumoto, H. Saito, T. Sekine, T. Ogawa, S. Morito, T. Maki, Phase transformation from fine-grained austenite, *ISIJ Int.* 48 (2008) 1038–1045.
 - [51] G. Miyamoto, N. Iwata, N. Takayama, T. Furuhara, Mapping the parent austenite orientation reconstructed from the orientation of martensite by EBSD and its application to ausformed martensite, *Acta Mater.* 58 (2010) 6393–6403.
 - [52] C. Lerchbacher, S. Zinner, H. Leitner, Atom probe study of the carbon distribution in a hardened martensitic hot-work tool steel X38CrMoV5-1, *Micron* 43 (2012) 818–826.
 - [53] N. Nakada, T. Tsuchiyama, S. Takaki, D. Ponge, D. Raabe, Transition from diffusive to displacive austenite reversion in low-alloy steel, *ISIJ Int.* 53 (2013) 2275–2277.
 - [54] O. Dmitrieva, D. Ponge, G. Inden, J. Millán, P. Choi, J. Sietsma, D. Raabe, Chemical gradients across phase boundaries between martensite and austenite in steel studied by atom probe tomography and simulation, *Acta Mater.* 59 (2011) 364–374.
 - [55] M. Kuzmina, M. Herbig, D. Ponge, S. Sandlöbes, D. Raabe, Linear complexes: confined chemical and structural states at dislocations, *Science* 349 (2015) 1080–1083.
 - [56] M. Kuzmina, D. Ponge, D. Raabe, Grain boundary segregation engineering and austenite reversion turn embrittlement into toughness: example of a 9 wt.% medium Mn steel, *Acta Mater.* 86 (2015) 182–192.
 - [57] F. Maresca, V.G. Kouznetsova, M.G.D. Geers, Reduced crystal plasticity for materials with constrained slip activity, *Mech. Mater.* 92 (2016) 198–210.
 - [58] G. Thomas, Retained austenite and tempered martensite embrittlement, *Metall. Trans. A* 9 (1978) 439–450.
 - [59] L. Yuan, D. Ponge, J. Wittig, P. Choi, J.A. Jiménez, D. Raabe, Nanoscale austenite reversion through partitioning, segregation and kinetic freezing: example of a ductile 2GPa Fe–Cr–C steel, *Acta Mater.* 60 (2012) 2790–2804.
 - [60] S. Morito, T. Ohba, A.K. Das, T. Hayashi, M. Yoshida, Effect of solution carbon and retained austenite films on the development of deformation structures of low-carbon lath martensite, *ISIJ Int.* 53 (2013) 2226–2232.